Non-destructive characterization of strain induced surface hardness increase by measuring magnetic properties of AISI 304

Stephan Krall, Markus Prießnitz *, Christian Baumann, Friedrich Bleicher

TU Wien, IFT - Institute for Production Engineering and Photonic Technologies

HIGHLIGHTS

- Phase transformation of AISI 304 stainless steel at room temperature caused by plastic deformation using the process of machine hammer peening.
- Localized mechanical energy input through machine hammer peening allows spatial influence of magnetic properties.
- Non-destructive testing of martensite content using different electromagnetic sensor technologies.
- Correlation between magnetic properties and mechanical hardness allows non-destructive hardness measurements.

GRAPHICAL ABSTRACT
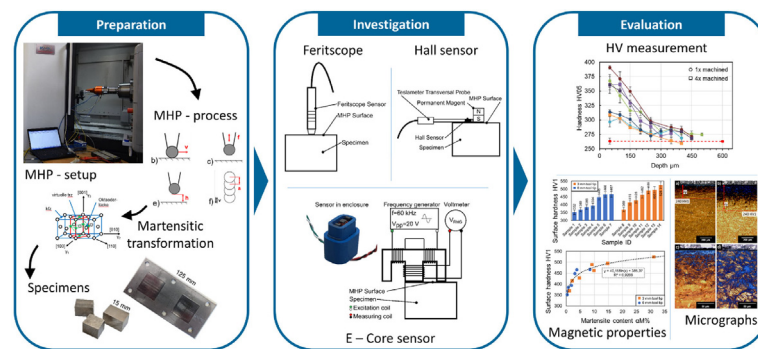
ABSTRACT

The goal of this work is to establish a correlation between the surface integrity and magnetic properties of stainless steels like AISI 304 (X5CrNi18-10). In metastable austenitic stainless steels, a phase transformation from the austenitic to the martensitic phase can occur even at room temperature. In this work, machine hammer peening (MHP) is used to selectively introduce the activation energy required for martensite formation on discrete areas of the surface. The phase transformation is confirmed by electron back scatter diffraction (EBSD) and micrographs. A correlation between the energy input by MHP, magnetic properties, and surface hardness is established. Using this approach, characterization of the surface integrity by measuring magnetic properties can be achieved. In addition, a novel solution to code and encode information with high information density onto metastable austenitic materials is proposed.

© 2023 The Author(s). Published by Elsevier Ltd. This is an open access article under the CC BY license (http://creativecommons.org/licenses/by/4.0/).

1. Introduction

1.1. Surface integrity and process signatures

The functional performance of a component and therefore its applicability is strongly influenced by its surface integrity, which is subsequently influenced by technology. Key metrics of the surface integrity include surface topography, microstructure, and mechanical properties [1]. In principle, these metrics usually occur in combination. However, it is possible to draw conclusions about a

* Corresponding author.
E-mail addresses: stephan.krall@tuwien.ac.at (S. Krall), markus.priessnitz@tuwien.ac.at (M. Prießnitz), christian.baumann@tuwien.ac.at (C. Baumann), friedrich.bleicher@tuwien.ac.at (F. Bleicher).

second property by measuring one of them. For example, the transformation of a material phase can have a direct influence on the material hardness.

According to Brinksmeier et al. [2], process signatures describe the relationship between the converted and dissipated energy of a process in interaction with a machined material. By the use of a manufacturing technology, the functional properties of a component are influenced at the surface and its boundary layers. The process signature assumes, that the energy provided and converted by the manufacturing process can be used to describe a specific change within the material. A process signature can also be used to predict machining processes in order to obtain defined functional properties. They are of particular interest if they are located in the layers close to the surface and can be influenced specifically.

1.2. Fabrication and verification of process signatures

Using a mechanical surface modification process like Machine Hammer Peening (MHP), in which the surface of the work piece is exposed to a high level of local plastic deformation, only a single cause-effect relationship is at play. The cause is the mechanical energy added into the workpiece material through its surface. A high force component results in a high deformation of the component and a greater dislocation activity within the deformed area occurs. The influenced effects are hardness, residual stress state, and the microstructure. These properties, which are anchored in the material, have the advantage that they are not only located on the surface, but extend to a depth of several hundred micrometers. Therefore, it is possible to change the properties inside the volume by just mechanical contact on the surface.

Values of residual stress states are difficult to measure, and depth hardness measurement also involves destructive testing, hence a simple way to more easily quantify these changes is of interest. One possibility to show the use of process signatures is the change of permeability in austenitic materials after local plastic deformation, i.e., measure the change in magnetic permeability caused by a stress-induced martensite transformation.

1.3. Machine hammer peening

MHP is a vibration-based surface modification processes that can be classified in the field of cold forming of materials. In combination with a machining system an MHP-actuator is guided over a workpiece surface. The reciprocal movement of the hammer head induces mechanical energy into the work piece. This influences the compressive residual stress state and can lead to work hardening within the surface near layers. In addition to these two effects, a modification of the workpiece topography, which can be classified in the category of surface smoothing or surface structuring takes place [3]. The tools typically consist of a hammer head made of carbide in the form of spherical caps. There are multiple options to generate the reciprocating movement. One option is an electrodynamic actuator (E-MHP system), which can be seen in a typical configuration in a machine tool in Fig. 4. Ghaednia [4] showed that plastic deformation occurs on the workpiece surface when the tensile strength of the indenter is at least 1.7 times that of the workpiece. During the contact between the hammer tip and the workpiece surface, elastic–plastic contact occurs. With a given mass of the movable tool, the hammer tip hits the workpiece surface with a defined kinetic energy. First, the peaks of roughness are deformed until the kinetic energy has been fully dissipated and elastic–plastic forming has occurred. The elastic part of the deformation causes a spring-back and the velocity of the hammer head is converted in the opposite direction. Finally, a plastically deformed surface with introduced residual compressive stresses remains.

To determine the energy input into the material, a combined approach of metrologically determined quantities and analytically determined values can be pursued. According to Johnson [5], defined parameters are responsible for the plastic deformation caused by the impact of a ball on a workpiece surface. They are the ball mass m_{WZ}, the geometric dimensions of the indenter, the impact velocity v_0 of the indenter as well as the material properties of the workpiece and the tool.

As friction and the deformation of the indenter are neglected, an approach according to Tabor et al. [7] helps to calculate the elastic energy E_E in the specimen. If the total (kinetic) energy E_{k0} exerted by the indenter on the workpiece is also known, the portion of the energy E_P that remains in the workpiece as plastic deformation can be calculated according to Equation (1).

$$E_P = E_{k0} - E_E \tag{1}$$

E_{k0} can be calculated using the Equation (2) for kinetic energy.

$$E_{k0} = \frac{m_{WZ} \cdot v_0{}^2}{2} \tag{2}$$

For the energy E_E, the radius r_2 of the remaining deformation observed on the workpiece must first be calculated (see Fig. 1 right). In the profile section obtained by a single impact, the diameter of the indention on the workpiece surface d_i and the depth t_p of the indentation are measurable. Using the geometric relationships on the circular segment, the radius r_2 is given by Equation (3).

$$r_2 = \frac{4t_p{}^2 + d_i{}^2}{8t_p} \tag{3}$$

Subsequently, the radius a_E (see Fig. 1 left) must be calculated, which is formed at the surface during purely elastic contact between the ball and the specimen. In order to calculate the radius a_E at the maximum of elastic contact, an approximation according to [7] is used in Equation (4). This equation assumes that the Poisson's ratio for both the indenter and the work piece material are equal.

$$a_E = 1.11 \left[\frac{F \cdot r_1 \cdot r_2}{2(r_2 - r_1)} \cdot \left(\frac{1}{E_1} + \frac{1}{E_2} \right) \right]^{\frac{1}{3}} \tag{4}$$

With the elastic energy E_E, given in Equation (5) [7], the energy of plastic deformation E_P can be calculated according to Equation (1).

$$E_E = \frac{0,27 \cdot F^2}{a_E} \left(\frac{1}{E_1} + \frac{1}{E_2} \right) \tag{5}$$

One phenomenon due to the MHP process is stress-induced martensite formation in metastable stainless steel [8,9]. An influence of the material phase of a metastable austenitic material by forming was investigated in [10] and [11]. The transformation of an austenitic-ferritic cast iron to a deformation-induced α'-martensitic microstructure using MHP processing was also demonstrated in [12]. Even for materials which are well tested and in use, like the aforementioned stainless steel 304, a characterization of surface integrity properties usually requires large and expensive equipment and are destructive hence not suited for production parts.

1.4. Magnetic properties and deformation induced phase transformation of stainless steel

Three basic types of magnetic behavior can be observed. These are distinguished by the relative magnetic permeability μ_r, which is the property of a material to be magnetized due to an external
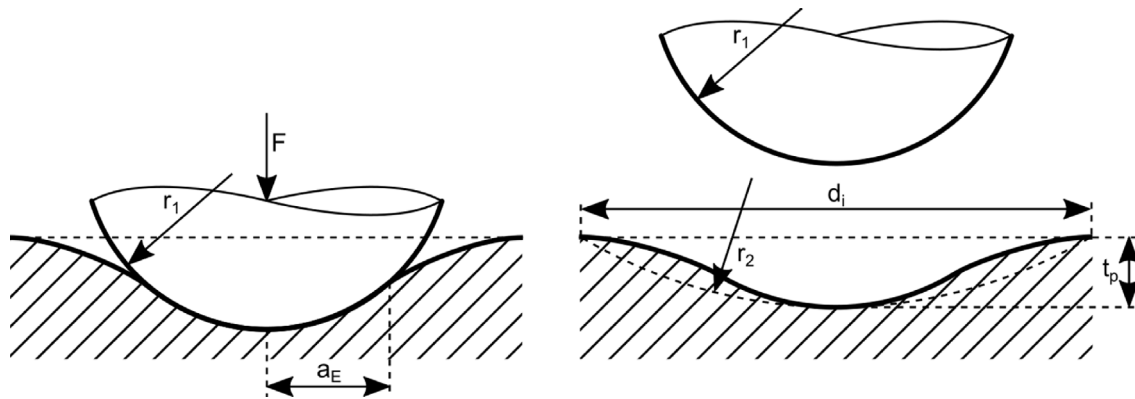
Fig. 1. Geometric sizes during (left) and after (right) the contact, according to [6].

field. They can be defined as diamagnetic ($\mu_r < 1$), paramagnetic ($\mu_r > 1$) and ferromagnetic ($\mu_r \gg 1$) material.

Ferritic stainless steel grades with a body-centered cubic lattice structure (bcc) such as X2CrNi12 (1.4003), X3CrNb17 (1.4511) and X6CrMoS17 (1.4105) exhibit soft magnetic behavior. Martensitic stainless steel grades (bcc) such as X12CrS13 (1.4005), X12Cr13 (1.4006), X14CrMoS17 (1.4104), X20Cr13 (1.4021), X46Cr13 (1.4034), X17CrNi16-2 (1.4057), and X15CrNi17-3 (1.4044) exhibit hard magnetic behavior, making them suitable as permanent magnets. In general, ferromagnetic properties can be controlled by different alloy compositions and heat treatments, [13]–[15]. In contrast, austenitic stainless steels (fcc) are diamagnetic and are therefore applied where neutral behavior towards magnetic fields is desired, for example in medical technology. Paramagnetic behavior is possible through the occurrence of deformation martensite (α'-phase) or through a ferritic residual structure after solidification (δ–ferrite). A certain ferrite content is often desirable, as it improves weldability and castability by reducing hot cracking tendency [14]. The austenitic phase of the microstructure of a metastable austenitic stainless steel needs to be stabilized to exist at room temperature. This can be done either mechanically through a volume increase during the cubic austenite to tetragonal martensite phase change or chemically by alloying with nickel, manganese, carbon, or cobalt. The phase change from austenite to martensite takes place without diffusion, the moving distance for each atom is less than the lattice constant. Transformation can occur at lower temperatures where diffusion is not possible. Phase transformations in metastable austenitic stainless can be induced thermally by supercooling or by applying external forces. In addition, a distinction between stress or strain/deformation can be made. Stress induced martensite transformation is characterized by an external stress below the yield point, where transformation by strain is caused by external stress above the yield point (introducing plastic deformation). The formation of deformation-induced α'-martensite induced by cold rolling of austenitic stainless steels is summarized in [16].This is depicted in Fig. 2 (a). The martensite transformation can be explained by the course of the free enthalpy G vs the temperature T. The relationship can be seen in Fig. 2 (b). Each system strives to assume a state of minimum free enthalpy. Above the transition temperature T_{trans}, the austenite is stable, because of the higher free enthalpy at higher temperatures. Below the transition temperature, the martensite has a lower free enthalpy and therefore is the stable phase. However, the transformation does not occur directly when the temperature falls below the martensite start temperature M_S: A differential enthalpy ΔG_S is necessary to initiate the transformation. At room temperature RT, ΔG_S can be applied by a combination of supercooling ΔG_{RT} and mechanically introduced enthalpy ΔG_{mech}.

If the sum of enthalpy due to supercooling down at room temperature and the mechanical enthalpy is greater than the necessary differential enthalpy, the transformation takes place instantly without diffusion, according to Equation (6).

$$\Delta G_{RT} + \Delta G_{mech} > \Delta G_S \tag{6}$$

The transformation process at the level of crystal structure can be described as follows: Considering the fcc structure, a virtually embedded tetragonal space centered cell (bct) can be recognized (Fig. 3 a). One description for a transformation from austenite (γ-phase) to α' martensite is provided by the model according to Bain [9] (Fig. 3).

The existing octahedral gap in the fcc structure merges directly into the octahedral gap of the martensite [17]. From this model, it can be seen that the {1 1 1} plane in the fcc structure corresponds to that of the {1 1 0} plane in the bct cell. Starting from this bcc cell, a deformation of the fcc cell must now be undertaken to obtain the structure of a martensite. This requires a compression of the fcc cell in the [0 0 1] direction by about 20.63 %, and an elongation in the [1 0 0] and [0 1 0] directions by 12.25 % [17] (Fig. 3 a). Due to an all-round deformation of the space cell which does not allow for a habit plane between the structures, the relationship according to Kurdjumov and Sachs is usually applied (Fig. 3 c). This relation suggests that there is an orientation relation between the {1 1 1} plane of the austenite and the {1 1 0} plane of the martensite as well as the [1 1 0] direction in the austenite and the [1 1 1] direction in the martensite [17]. In addition to the difference in strength from austenite to martensite, the increase in volume due to the phase transformation is also important when modeling these materials. The volume change during the phase transformation, caused by the density difference from austenite to martensite, is a concomitant of the strength-increasing martensite formation. This effect or transformation is often referred to as transformation-induced plasticity (TRIP) [18]. This transformation mechanism can be observed in austenitic materials after plastic forming. This plastic deformation caused leads to strain hardening effects and influences the grain size. An increase in strength can be attributed to the increasing dislocation density in the crystal structure as well as to fine grain refinement [19]. As an example, the following austenitic stainless steels, given in Table 1, are suitable for deformation-induced martensite formation [13,14,20], where the material AISI 309Si show a lower amount of α' martensite after rolling compared to AISI 304 [21]. The material which is used in the experiments is marked with a *.

Depending on the forming degree φ (Equation (7)), the magnetic conductivity of the material changes and thus its relative permeability [15]. The change in permeability for some stainless steel materials related to their forming degree are listed in Table 2.
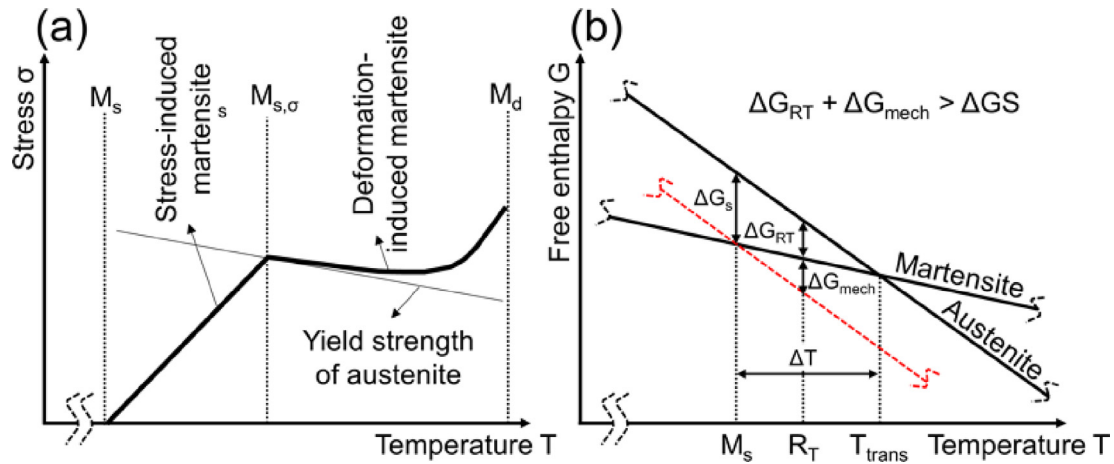
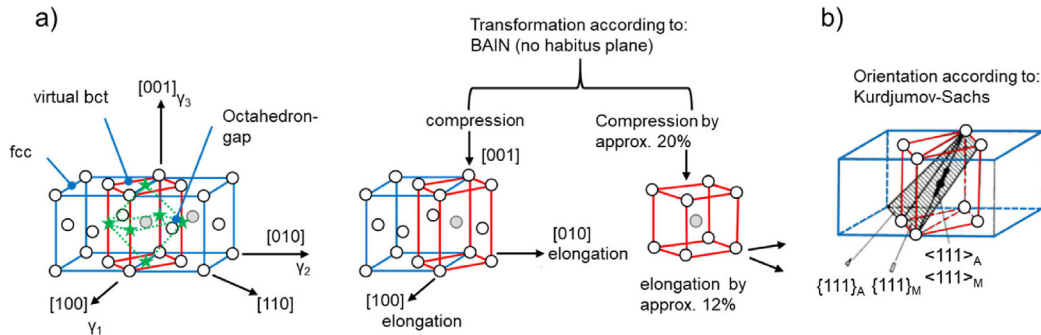**Fig. 2.** (a) Stress and (b) free enthalpy related mechanisms of martensite transformation.

Fig. 3. Phase transformation of CrNi steels according to Bain (a), Kurdjumov and Sachs (b) [18].

Table 1
Chemical composition in wt% of stainless steel for which deformation-induced martensite formation is possible.

Material	C	Cr	Ni	Mn	others
X5CrNi18-10 (AISI 304)*	0.038	18.16	9.04	1.34	–
X8CrNiS18-9 (AISI 303)	0.100	18.00	9.00	2.00	–
X2CrNiMo18-14–3 (AISI 316 L)	0.030	18.00	14.00	2.00	3 (Mo)
X3CrNiCu18-9–4 (AISI 304 Cu)	0,04	18	9	2	4 (Cu)
X15CrNiSi20-12 (AISI 309Si)	0.050	20.00	11.50	0.85	1.90 (Si)

Table 2
Permeability after cold forming with different forming degrees φ [15].

Grade	φ = 0	φ = 0,1	φ = 0,2	φ = 0,3
X8CrNiS18-9 (AISI 303)	1.003	1.050	1.620	3.420
X5CrNi18-10 (AISI 304)	1.012	1.046	1.626	3.090
X2CrNiMo18-14–3 (AISI 316 L)	1.007	1.008	1.024	1.130
X3CrNiCu18-9–4 (AISI 304 Cu)	1.005	1.005	1.012	1.082

The forming degree φ is defined as the logarithmic ratio of the change in shape compared to the original shape. In the case of spherical indentations, φ can be calculated using Equation (7).

$$\varphi = ln \frac{d_i}{2a_E} \tag{7}$$

As can be seen in Equation (7), the degree of deformation is calculated from the logarithmic ratio between the radius left behind by the indenter (0.5 d_i) and the radius a_E. r_2 can be calculated according to Equation (3), compare to section 1.3. a_E is the radius of the area of purely elastic contact at yield (see Fig. 1, Equation (4)).

1.5. Objective and novelty

The objective of this research is to investigate the effects of stress induced martensite formation by machine hammer peening on austenitic stainless steel materials. The novelty is the correlation between destructive and non-destructive measurement principles. This opens up the possibility of non-destructive characterization of surface hardness through magnetic properties. Furthermore, a novel approach to apply and read magnetic codes to the materials' surface is presented.

2. Materials and methods

2.1. Experimental apparatus and tools

MHP experiments were conducted on a 4-axis CNC milling machine (DMG Mori Seiki NHX 6300, Japan). Fig. 4 shows the experimental setup including the used sensor devices (force, displacement) for the actuator. The surface treatment was done using an electro-dynamic actuator system (Accurapuls, Germany). An AC-signal in a range of 20 – 500 Hz is applied to the coil [15,22]. The actuator is mounted in the machine tool spindle via a BT50 interface. Two different tool tips were used: half spheres with a diameter of d = 3 mm and 6 mm, made out of tungsten carbide (WC-Co). The setup and the working principle of the actuator can be seen in Fig. 4. The measurement probes (force, displacement) are fixed to the machine table and the actuator system, respectively.

2.2. Materials

AISI 304 is the most commonly used stainless steel in a variety of applications. Martensite transformation is a factor when working with AISI 304, especially in welding or cold forming processes like deep drawing. Therefore, a simple solution to determine surface integrity of this material is of great benefit when it comes to phase transformations. The material used in this work is a 10 mm steel sheet of AISI 304. In Table 1, the chemical composition of the material used is given in the first row. The material is quenched and drawn with a yield strength of 329 N/mm^2 according to the datasheet included with the material, a mean hardness value of 263 ± 5 HV05, and a surface roughness of Ra = 0.3 μm. Hardness and roughness measurements were performed on material from the initial 10 mm sheet material in house.

2.3. Validation methods of process integrity

In order to determine effect of MHP on the surface integrity, a characterization of the specimens is conducted using Vickers hardness tests, micrographs, and electron backscatter diffraction (EBSD). Hardness tests were conducted using a Vickers diamond indenter (EMCO, Austria) set to HV05 (load = 4.9 N) with a load application time of t = 15 s. The hardness measurements were performed on cross-sections with indents made from the top surface into the material with a minimum indent spacing of 50 μm. In order to avoid hardening effects induced by prior hardness measurements, a zig-zag pattern for the single hardness indents was used. Surface hardness was measured using a Krautkramer MIC

20 (General Electric, USA) hardness tester in conjunction with its HV1 (load = 9.81 N) measurement probe. Micrographs were made to evaluate the phase distribution due to the influence of deformation after the surface treatment. The color etching method Lichtenegger-Bloech (LBI) was chosen. With this etching method, different phases including martensite and delta ferrite can be observed. Images were taken using a microscope Axioplan (Zeiss, Germany). In addition, an electron backscatter diffraction analysis was performed, using a Quanta 200 FEG (FEI, USA), to gain a better understanding of the phases present in the surface-near areas.

2.4. Validation of process integrity using magnetic properties

Next to classical methods, the change of the SI can be verified by measuring the magnetic properties. The acquisition of magnetic properties offers the possibility to detect the effects of permeability change. Different measuring methods can be used for this purpose. In general, these measuring methods are called magnetometers. Magnetometers measure the magnetic flux density, from which the permeability can be determined. However, it is also possible to measure the magnetic permeability directly. In the context of martensite transformation, the measurement of permeability is of particular interest, since the deformation-induced martensite formation occurring during MHP directly affects the magnetic permeability. In order to describe the transformation via the magnetic properties, three measurement techniques are investigated in this work: A commercially available Feritescope, magnetic flux of a static field using a Teslameter, and a low-cost differential measurement technique using a high frequency alternating field. Due to the microstructure composition, untreated austenitic stainless steel (such as baseline AISI 304) shows diamagnetic behavior. By evoking a martensite transformation, ferromagnetic deformation martensite (α'-phase) forms; the affected areas now show ferromagnetic behavior. The magnetic permeability is proportional to the amount of α'-martensite and thereby to the energy input due to MHP. By that the determination of surface integrity using magnetic properties is possible, which is shown in Section 3.2.

2.5. In process force and position measurements

The forces acting between the hammer head and the workpiece during the MHP process were measured using a three-axis dynamometer (Kistler 9129AA, Switzerland), and the hammer head movement was determined using an eddy current sensor (Micro Epsilon NCDT 3300, Germany). Using this equipment, it is possible to determine the force during forming as well as the veloc-
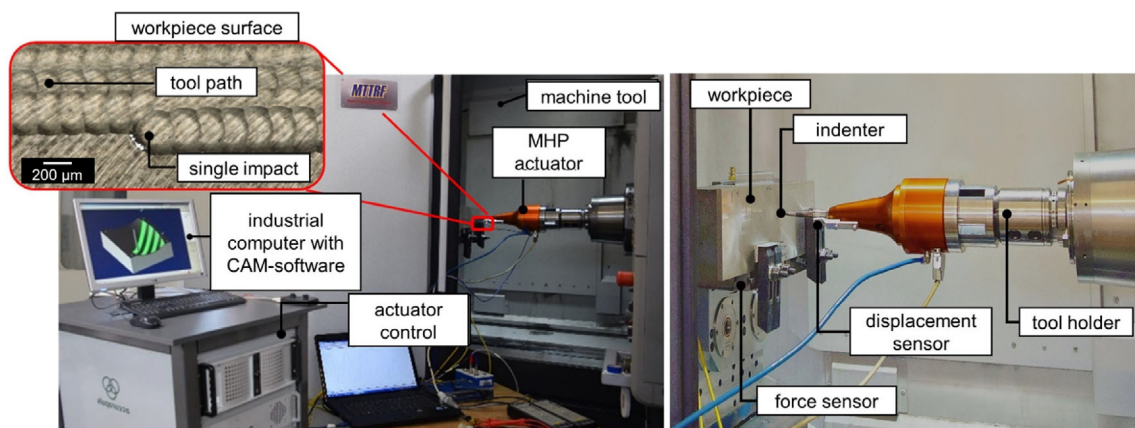

Fig. 4. Experimental setup for MHP.

ity of the hammer tip. With this, the energy before impact on the workpiece surface can be calculated (compare to Section 1.3).

2.6. MHP-Surface treatment procedure

In order to obtain the maximum effect of transformation of γ-iron to α'-phase by plastic deformation caused by MHP, the influence of multiple surface treatment passes was investigated. Surface roughness, as one quality indicator, could indicate a negative effect for very high energy input. Higher induced plastic deformation due to multiple peening passes leads to a breakup of the surface and therefore to an increase of the surface roughness. The surface roughness was measured perpendicular to the machined direction as this shows a higher value of R_a. The parameters used show an increase of the surface roughness after machining the same area five times (Fig. 5). Based on this, the maximum number of machining was set to n = 4, so that the estimated surface roughness decreases to a minimum value.

Other parameters used for the MHP treatment were set to commonly used values and are given in Table 3.

The symbols in Table 3 are named according to VDI 3416 [3]. Combining both parameters v and f, according to Equation (8), the distance of indentation (symbol a) can be calculated. The dependency between the hammering frequency f in Hz and the feed rate v in mm/min is given by the distance of indentation a in mm, which specifies the spacing of the individual indentations in the feed direction.

$$a = \frac{v}{60 \cdot f} \qquad (8)$$

By the given process parameters, the contact force between the hammer tip and the workpiece surface can be measured using the stationary dynamometer and the movement of the hammer tip with an eddy current sensor. The single impacts were imaged using a white light optical metrology system InfiniteFocus® G4 (Alicona, Austria). At this point, a total of 14 specimens with varied energy input and thereby varied strain-induced martensite content are present and are investigated.

3. Results

3.1. Validation of the MHP process

The evaluation of the hammer head motion shows a higher contact time at small stroke with h = 0.3 mm than at h = 0.8 mm. This is due to the actuator principle and implies that no optimum stroke can be achieved. This fact could also be confirmed by [23]. In this case, a contact time of around t = 1.4 ms can be determined for a stroke of h = 0.3 mm. In contrast, the contact time of the hammer head h = 0.8 mm is about t = 453 μs. The motion curves shown in Fig. 6 are filtered with a cut-off at 1200 Hz.

Based on this motion profile, a velocity profile can be calculated by the first time derivative (d_x/d_t). From this, the maximum veloc-
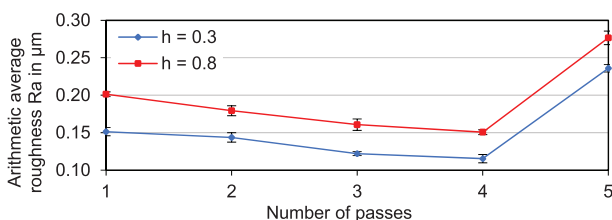
ity and thus the kinetic energy with an oscillating mass of m = 0.424 kg at the impact can be determined (Table 4).

In Fig. 7, the results of the contact force measurements between the oscillating hammer tip and the substrate are shown. In addition to the used parameters for the stroke h which are marked in blue, different parameters for the stroke and their results are given. The results have been averaged over the tool path, and the standard deviation for all conditions is within ± 25 N.

Using the Equations (1) - (3), the energy to be applied for the plastic deformation can be calculated. It is to be mentioned that the last two equations are based on a Poisson's ratio of 0.3 for the indenter and the workpiece. The results of the calculated plastic energies E_P and the elastic energy components E_E are summarized in Table 5. These energy quantities calculated here show that when the larger stroke h = 0.8 mm is selected, a factor of 4.8 higher energy is introduced into the material surface than with a smaller stroke of h = 0.3 mm. With Equations (4) - (7), the forming degree φ and the geometrical conditions at purely elastic impact can be calculated. Using the radius of the indenter r_1, a Young's modulus of 215 MPa for stainless steel 304 [24] and 550 MPa for WC-Co [25], the contact radius a_E is calculated using Equation (4). Other parameters were taken from measurements (Table 4, Table 6).

In Table 7, the calculated forming degrees φ (Equation (7)) are shown for h = 0.3 and h = 0.8 mm. The values for φ achieved here are about two time higher than the values listed in Table 2. This means high plastic deformation occurs when using MHP as a surface modification process.

It is to be noted, that the forming degree for the longer stroke h = 0.8 mm results in a lower forming degree than the shorter h = 0.3 mm stroke. This is against intuition, since the longer stroke contains a higher impact energy E_{k0}, which in theory should result in a higher forming degree. However, the martensite formation below the hammer head leads to instantaneous hardening, counteracting further deformation. This is also confirmed by the hardness measurements in Fig. 8 and Fig. 9, which consistently show higher hardness values for the longer stroke when the other peening parameters are the same.

4. Measurements of surface integrity

4.1. Surface hardness measurements

Fig. 8 shows the measured Vickers surface hardness. Specimens are sorted in ascending order by their energy input and grouped according to the tool tip diameter. Hardness increases with more energy input due to more martensite being formed, and the samples prepared with the 3 mm tool tip (marked in orange) show higher hardness values for the same processing parameters. Hardness of the untreated reference specimen was measured at 240 HV1. This means a hardness increase between 47 % (Sample 1) and 119 % (Sample 14) compared to the baseline can be achieved. This behavior is expected, since for a given force a smaller diameter tool exerts more strain on the specimens, thereby introducing more ΔG_{mech}, ultimately forming more of the harder martensitic phase.

4.2. Hardness profile measurements

Hardness profile measurements were performed according to VICKERS. Penetration depth t_p – the distance from the surface where the measured hardness corresponds to the baseline (surface) hardness of a reference specimen – was found up to 800 μm for the specimens prepared with the 3 mm tool tip and 450–500 μm for the ones prepared with the 6 mm tool tip. Starting

Fig. 5. Break-even of surface roughness after multiple MHP passes; v = 1200 mm/min, f = 200 Hz, d = 3 mm, s = 0.1 mm.

Table 3
MHP parameters for experiments.

SN	1	2	3	4	5	6	7	8	9	10	11	12	13	14
v	2400				1200			2400				1200		
a = s	0.2				0.1			0.2				0.1		
h	0.3	0.8	0.3	0.8	0.3	0.8	0.3	0.3	0.8	0.3	0.8	0.3	0.8	0.3
n	1	1	4	4	1	1	4	1	1	4	4	1	1	4
d	6							3						
f	200													

SN…sample number; v…feed rate (mm/min); a…distance of indentation (mm); s…stepover distance (mm); h…stroke (mm); d…diameter of tool (mm); n… repetition of machining; f… hammer frequency (Hz).
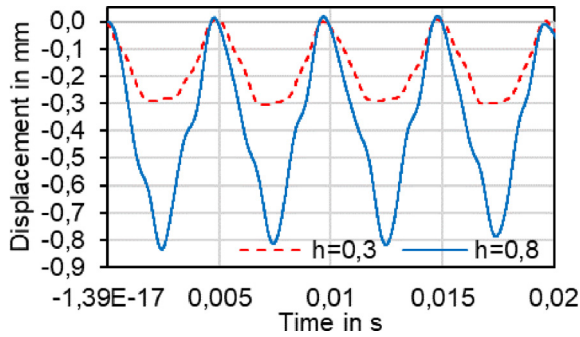
Fig. 6. Displacement of hammer head at different stroke and f = 200 Hz.

Table 4
Results of force and displacement measurements and calculations.

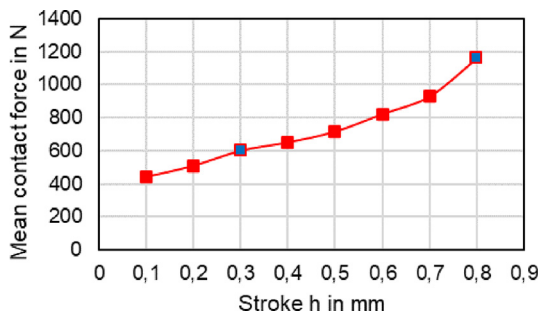| stroke h in mm	contact force F in N	v_0 in m/s	kinetic energy E_{k0} in mJ
0.3	628	0.24 ± 0.03	12
0.8	1159	0.53 ± 0.04	58

Fig. 7. Mean contact force for d = 3 mm and stainless steel 304 at f = 200 Hz.

Table 5
Calculated elastic and plastic energy influenced by the stroke h.

	h = 0.8 mm	h = 0.3 mm
plastic energy E_P in mJ	48.15	7.88
elastic energy E_E in mJ	10.27	4.33
Initial kinetic energy E_{k0} in mJ	58.42	12.21

from a base hardness of the material of 263 ± 5 HV05, a separation is made between the single machined and the multiple machined

Table 6
Image and properties of dents after single impact with d = 3 mm.

h in mm	depth of indent t_p in µm	diameter of indent d_i in µm
0.3	15.9 ± 1.1	775 ± 18.7
0.8	22.9 ± 1.0	876 ± 14.4

Table 7
Forming degree φ achieved by MHP using a hammer head diameter d = 3 mm.

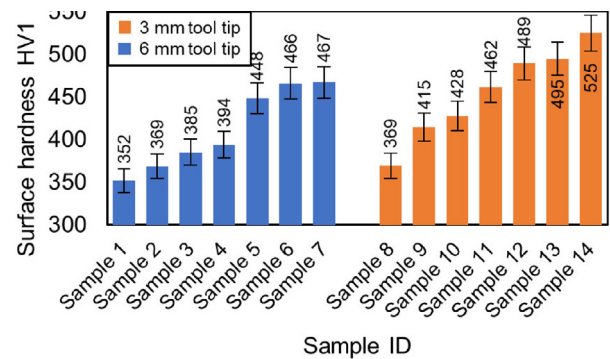| φ for h = 0.3 mm	φ for h = 0.8 mm
0.72	0.65

Fig. 8. Results of surface hardness measurements according to Vickers HV1.

specimens. It can be seen that the results of the hardness measurements depend considerably on the energy applied, which is influenced not only by the stroke but also by the hammer head diameter. It can be seen that the samples 12 to 14 show the highest increase in hardness. It is also evident that multiple machining passes increase the hardness. Sample No. 14 shows the highest hardness values (468 HV05). The maximum measured hardness of this machined specimen is 1.8 times higher than the base material. Sample 13 shows the highest penetration depth, close to 750 µm.

4.3. Micrographs

In Fig. 10 micrographs were produced to evaluate the phase distribution. Three different samples, specimen No. 7 which is shown in a) and c); specimen No. 14 is depicted in b) and d) and an untreated reference specimen displayed in e), are shown. For the specimen No. 7 and No. 14 two different tool tips (3 mm and 6 mm) were used. The samples were cross-sectioned in the middle of the area to observe the microstructure when the process is in a steady state. The LBI etchant was used to add color to the images and highlight different phases: e.g., martensite, delta ferrite. Fig. 10 e) shows the microstructure of the reference specimen, in the initial state, from base material (bottom) up to the near surface region (top). It shows a typical microstructure of an austenitic stainless steel with a homogeneous microstructure.

The MHP-treated specimens Fig. 12 a) - d) show the different phases very clearly. An area of high deformation is clearly visible. The austenitic phase is shown in yellow to orange hues, whereas the martensitic phase appears blue. The MHP-treated surface exhi-
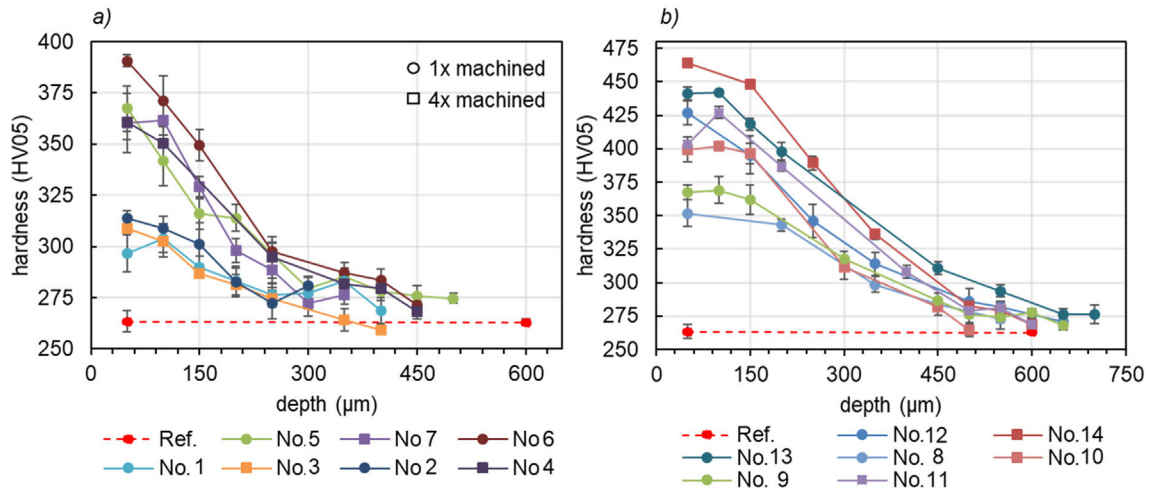
Fig. 9. Results of hardness measurements according to Vickers HV05: a) hardness profile using a 6 mm hammer tip b) hardness profile using a 3 mm hammer tip.
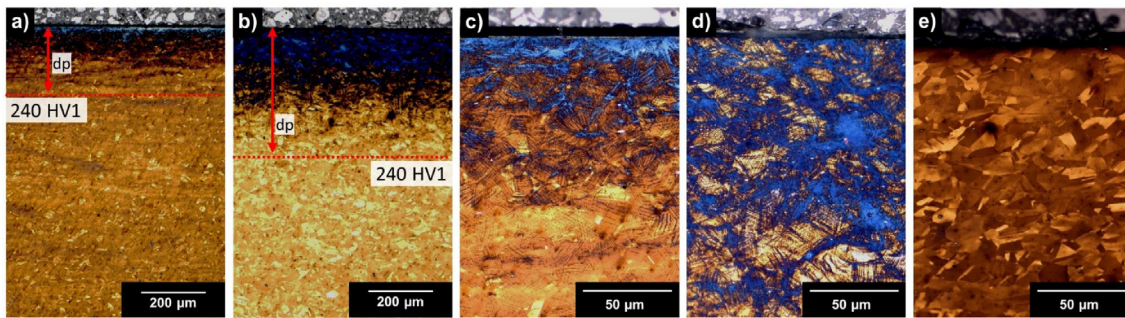

Fig. 10. Cross-section of treated sample No. 7 (a), sample No. 14 (b), zoomed view of sample No. 7 (c), zoomed view of sample No. 14 (d), zoomed view of untreated baseline sample (e).
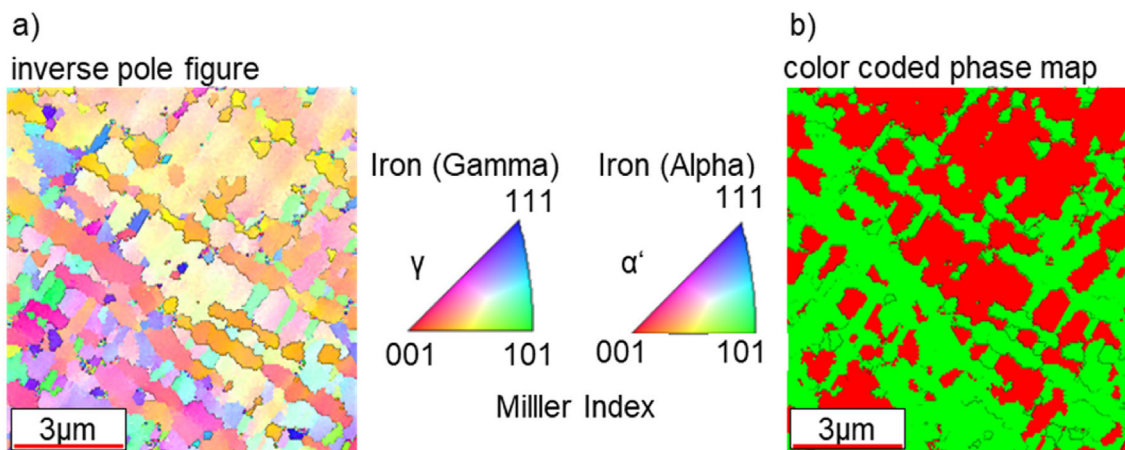

Fig. 11. EBSD analysis: IPF and CCM for sample treated with the maximum energy, a) inverse pole figure, b) color coded phase map.

bits martensite near the surface area, and the maximum depth of martensite transformation increases with more energy introduced and appears as a highly deformed grain structure with high dislocation density. This grain structure can be observed over the entire penetration depth d_p and fits well with the hardness profile measurements of section 3.2.2.

When using the large tool tip, as shown in Fig. 10 a) and c), i.e. lower energy input, a near-surface microstructure transformation results. The deformation intrudes up to a height of about 200 μm

from the surface. Whereas with the small tool tip (specimen No. 14), which generates a higher energy input, a much greater effect in depth can be observed. This is shown by an approximate penetration depth of 400 μm.

4.4. Electron backscatter diffraction

Due to the high dislocation density caused by MHP in the near surface region, it can be difficult to identify the phases in the
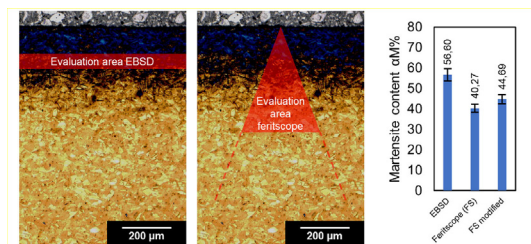
Fig. 12. Evaluation area of EBSD and feritscope, α'–martensite values.

surface-areas correctly using only color etching techniques. Therefore, a sample with a maximum of plastic deformation was prepared and afterwards investigated by EBSD. For this, a specimen was peened with the parameters of sample No. 13 (see Table 8) Table 3, but with a number of repetitions of n = 4. This new specimen is denoted as sample No 15. The description of the abbreviations and symbols can be used from Table 3.

A small sample of 15 × 15 mm was taken from the treated material sample, using a wet cutting machine, and it was examined in the scanning electron microscope at an angle of 70°. The specimen was then evaluated at a depth of 160 μm beyond the MHP-treated surface within an area of 3 μm² at 15 KV accelerating voltage. For the EBSD scan, a step size of 200 nm was used to scan the measurement field. Fig. 11 a) shows the inverse pole figure (IPF) including the color key and Fig. 11 b) the color-coded map (CCM) of the investigated specimen. The specimens were embedded in a conductive mold for analysis. In the final step, chemical fine polishing was performed. The samples were additionally contacted by a carbon tape.

The IPF is used to identify the orientation of the crystal structure. The color key is given in the center of Fig. 16 where each corner point corresponds to an orientation of the crystal structure. By assigning the three colors, red, blue and green, it is possible to visually indicate the exact orientation. If one face of the crystal lattice is parallel to the {1 0 0} plane, this area is displayed in red. For the case of an edge parallel to the {1 1 0} plane the area is colored green and a parallel corner to the {1 1 1} plane is colored in blue. The color gradients show a mixed orientation of the crystals. The IPF of the 3 mm-category shows highly deformed structures and deformation patterns in it. In contrast, the CCMP shows a color associated with the material phase. The CCPM shows a high fraction of strain induced α'-martensite marked in bright green. Gamma iron, which is representing the austenitic phase, is shown in red color. Strikingly, the microstructure is noticeably inhomogeneous, forming a series of parallel and intersecting bands of α'–martensite. It can be seen that the strain-induced α'–martensite is preferentially formed at the intersections. Analyzing the grain size of the α'-martensite indicates fine-grains with an average diameter of about 1 μm. Between intersecting bands of the α'–martensite phase, a difference in angle of about 95° can be observed by image inspection. According to [26], martensite needles are preferably formed at an angle of 60° to 120° to the last needle and are limited in extent by the needle(s) and/or austenite grain boundaries. If the CCPM is evaluated with respect to the color components via pixel analysis, a proportion of the forming martensite in the range shown here of 56.6 % can be determined. Accordingly, a remaining austenite content of 43.4 % exists. Of course, it must be noted that

only a small area was investigated with EBSD in a certain depth. When checking the color etched cross-sections of the previous treated samples in Fig. 10, the martensite does not fully cover the planar surface. Based on this, the content of martensite mentioned above represents a local area below the MHP-treated surface and does not necessarily match the overall microstructure of the specimen.

4.5. Measurements of ferrite content

An option to detect the ferritic phase fraction in a non-destructive test setup is the measurement with a commercially available feritscope, namely the Feritscope FMP30 (Helmut Fischer GmbH, Germany). It works using a magneto-inductive method: A coil is excited with a low-frequency of about 168 Hz and generates an alternating magnetic field which interacts with the sample [27]. Depending on the interaction, a voltage is induced in a second coil, which is related to the ferrite content. One typical field of application is weld seam testing. By applying a correction factor, the feritscope can be used to detect the martensitic α'–phase fraction. The implemented ferrite to α' conversion is based on work by Talonen et al. [28]. The readings of mass % δ -ferrite are converted to mass % α'-martensite by multiplying a factor of 1.7. Based on Fava et al. [29], a calibration curve can be used to convert the mass % δ -ferrite to mass % α'-martensite for highly deformed areas. By applying this non-linear calibration curve to specimen No. 15, which shows a maximum of plastic deformation, the mass % δ -ferrite reading increases about 9.9 % from α'-martensite content of 40.27 % to a value of 44.69 %, as can be seen in Fig. 12, where the evaluation areas of the EBSD and the feritscope are also shown schematically. It has to be noted, that the EBSD analyzes a specific area on a prepared surface, whereas the feritscope measures a 3-dimensional cone with a higher penetration depth. Therefore, the α'-martensite content measured using these two techniques are not directly related to one another.

As it is mentioned by Fava et al., the linear conversation based on Talonen et al. [28] is valid for readings below 30 % of mass % δ -ferrite. By that, the linear conversation by the factor of 1.7 is acceptable for the measured values in this study. Fig. 13 shows the martensite content, and Fig. 14 the correlation of the martensite content to the surface hardness using the feritscope. Of all the non-destructive measurement methods presented in this work, this is the most recommended process for two reasons: First, a direct measurement of the martensite content is possible due to the correction factor determined in the preceding work mentioned above. Second, a correlation to the surface hardness with a very high R^2-value of 0,93 is possible. The formula as well as the exact R^2 value is given in the dotted box in Fig. 13. Specimens that were processed using the 3 mm MHP tool tip are marked in orange, the ones processed with the 6 mm half sphere are marked in blue. This is true for all following plots. In Fig. 13, specimens are ordered by energy input and grouped according to tool tip diameter. As can be seen, the martensite content increases exponentially with higher energy input. This is the reason why a logarithmic regression function is used in Fig. 14. When using this logarithmic function to calculate back to the surface hardness, a mean relative error of −6,22 % is achieved.

Table 8
MHP parameters for the sample investigated by EBSD.

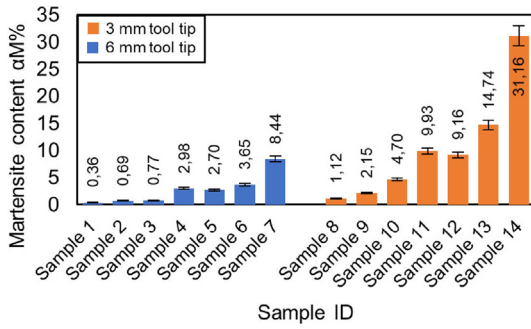| SN	v	a = s	h	n	d	f
15	1200	0.1	0.8	4	3	200

Fig. 13. Results of martensite formation after MHP treatment using the feritscope.

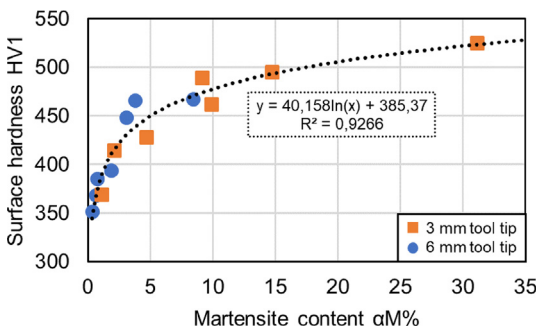**Fig. 16.** Correlation between surface hardness and the Teslameter data.

is certainly possible, but with the setup and alternatives presented in this work not the preferred option.

4.7. Magnetic field measurements

The sensor system used in this section operates on an electro-magnetic principle. An E-core made of soft magnetic material is equipped with an excitation coil consisting of two windings and a measuring coil. The sensor system is mounted in a spring-loaded enclosure. This arrangement is similar to Barkhausen sensors. The excitation coil is excited with a high-frequency sinusoidal alternating voltage (60 kHz, 20 V_{pp}). This creates an alternating magnetic field which flows through the legs of the core. The alternating field induces a voltage in the measuring coil. The induced voltage is the output signal of the sensor and is recorded with a voltmeter as RMS value. Fig. 17 and Fig. 18 show the correlation of the E-core measurements to the martensite content and the surface hardness. As can be seen in Fig. 17, a high correlation between the voltage measurement values and the martensite content is achieved using a linear fit. For surface hardness, the same statements made for the Teslameter are true as well: low R^2-value, and a better fit when splitting into two datasets. However, this sensor still provides the second recommended measurement technique as a two-step process: obtain martensite content using the E-core sensor. From there, use the correlation of martensite content to surface hardness given in Fig. 14. This yields a mean relative error of 5,99 % when calculating back to the surface hardness.

4.8. Deployment of process signatures

The dissipated energy of the MHP process leads to a plastic deformation on a deformable material and the amount of energy is influencing the material properties. With the gained knowledge in the field of the MHP as well as in techniques for surface integrity measurements, it is possible to use this information to add new
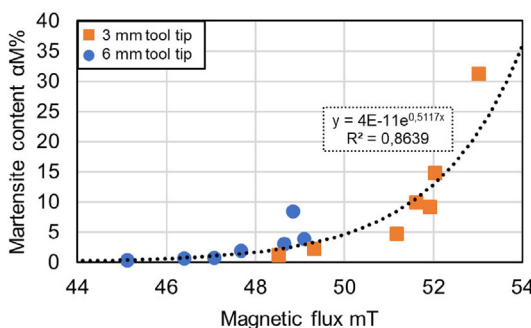

Fig. 14. Correlation between surface hardness and feritscope data.

4.6. Electromagnetic field measurements

A Teslameter model FM 302 (Projekt Elektronik GmbH, Germany) is used in combination with its transversal probe to detect magnetic field properties. A Hall sensor integrated in the tip of the probe measures the magnetic flux. A strong neodymium permanent magnet is used to provide the magnetic field which is altered by the magnetic permeability of the specimen, and in turn picked up by the Hall sensor. When using the Teslameter, an exponential behavior of the measurement values can be observed (Fig. 15, Fig. 16). Correlation to the martensite content is good with R^2 of 0,86, however surface hardness shows a R^2-value of only 0,75. This may be acceptable for some applications, but is among the lowest values observed in this investigation. Here, splitting the dataset according to the used tool tip diameter yields far higher R^2-values (0,95 for 3 mm tool tip, 0,91 for 6 mm tool tip). However, since peening parameters or even the cause of the martensitic phase transformation may not necessarily be known, the broad approach using all datapoints for one correlation function is chosen. To sum up, surface integrity determination using a Teslameter

Fig. 15. Results of martensite formation after MHP treatment using the Teslameter.
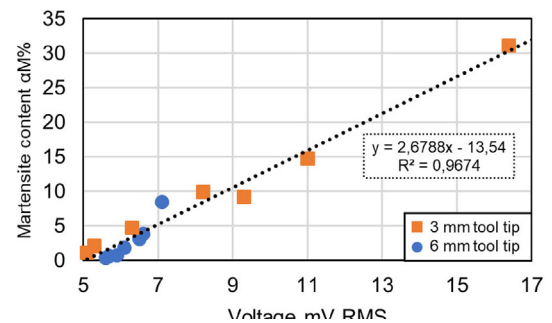

Fig. 17. Results of martensite formation after MHP treatment using the E-core sensor.
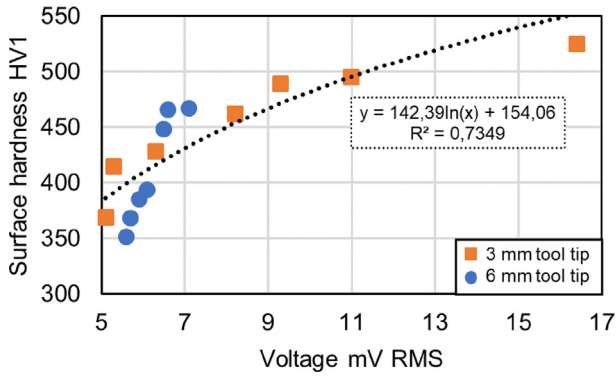
Fig. 18. Correlation between surface hardness and data from E-core sensor.

Fig. 20. Results of E-core sensor measurements of different materials.

features to a material or to a workpiece. In this section, the MHP process and the sensor from section 3.2.7 are used to show a simple form of coding and encoding for metastable austenitic materials, in this example a sheet of stainless steel.

The material used in this section is a 2 mm stainless steel sheet of type AISI 304. The composition as well as the mechanical properties are close to the thicker plate used before. The sheet metal was peened with the most suitable MHP parameters in order to optimize the effect of increased permeability. In Fig. 19, the evaluation procedure for measuring the magnetic properties is shown.

When measuring the static voltage level using an E-core (Fig. 20), it is noticeable that the measured values are indirectly proportional to the magnetic permeability. These measured values are determined statically on the surface of the sample or the ferrite and aluminum sheet.

The measurements were performed with continuous feed. Fig. 21 shows an exemplary schematic course of such a measurement plot. It should be noted that the raw data of the measurement signal are in the form of voltage–time datapoints. The known (constant) feed rate can be used to calculate back to the traverse path. Thus, the measurement curve is available as a voltage-distance figure. Fig. 21 shows 13 areas with a linear course. Each of these areas can be assigned to a unique event.

The events of the individual fields are explained below:

1. the sensor is completely outside the treated area.
2. the first leg of the core passes the edge
3. the first gap of the core passes the edge
4. the second (middle) leg passes the edge
5. the second gap passes the edge
6. the third leg passes the edge
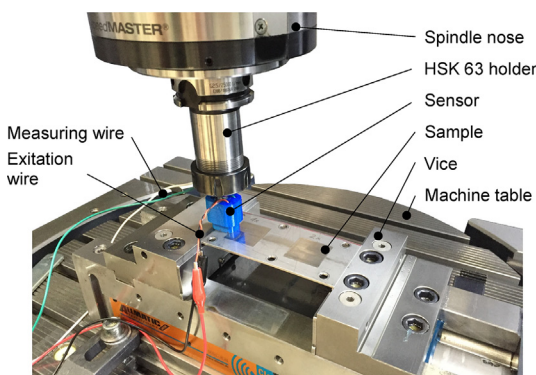7. the sensor is completely inside the processed field

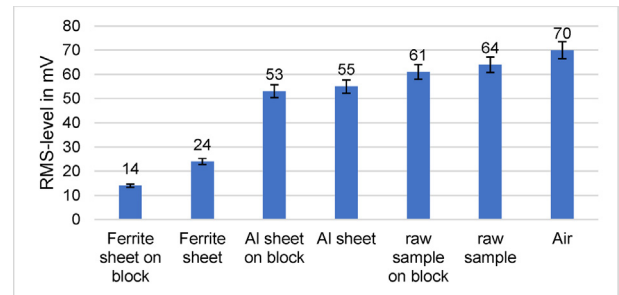**Fig. 19.** E-core sensor head and measurement setup.

8. the first leg passes the opposite edge of the field
9. the first space passes the opposite edge of the field
10. the second (middle) leg passes the opposite edge of the field
11. the second (middle) leg passes the opposite edge of the field
12. the third leg passes the opposite edge
13. the sensor is (again) completely outside the area

In Fig. 22, the measurement results of the stainless steel sheet with the fixture block as a base are given. In order to show the evaluation of a barcode in a simplified format, the results of the single and the double processed field are shown. The entry and exit of the fields can be clearly seen from the peaks. An indication which of the fields is currently being scanned can be made by the size of the peaks. As can be seen, multiple processing leads to higher energy input and thus to a changed magnetic conductivity. This can be easily visualized via the E-core sensor system. The information introduced into the material here makes it possible not only to display a binary bar code, but also to realize an additional information level via the intensity of the machining. This allows the data density of the bar code to be increased. As described in Section 3.2.2, this information can be written up to 750 μm below the surface.

5. Discussion

The influence of multi-processed MHP on the deformation-induced martensite formation and the resulting increase in surface hardness could be demonstrated in detail. The material X5CrNi18-10 (AISI 304) has a high tendency to work hardening. An increase in plastic deformation at the material surface also increases the proportion of the deformation-induced α' phase (martensite). Furthermore, it could be shown that a paramagnetic material behavior exists at the surface of the peened areas and that this can be enhanced by increasing the plastic deformation. The enhanced permeability could subsequently be described by means of suitable sensor technology and measurement methods. With the aid of several electromagnetic measurement methods, the intensity of the process can be derived from the increase in magnetic permeability. Furthermore, with a modified sensor design, it is possible to detect the edge transitions between unpeened and peened areas by a continuous measurement process. This makes it possible to assign a characteristic measurement signal curve to a peened field as a function of its size and its magnetic permeability. However, it has to be noted, that the feritscope tends to underestimate the a'-martensite. A calibration curve has to be applied to obtain actual a'-martensite content [28], as the used ferrit scope had it. In addition to classical methods such as hardness determination or EBSD analysis, it is possible to quantify the transformation and the mechanical properties non-destructively using electromagnetic measuring methods.
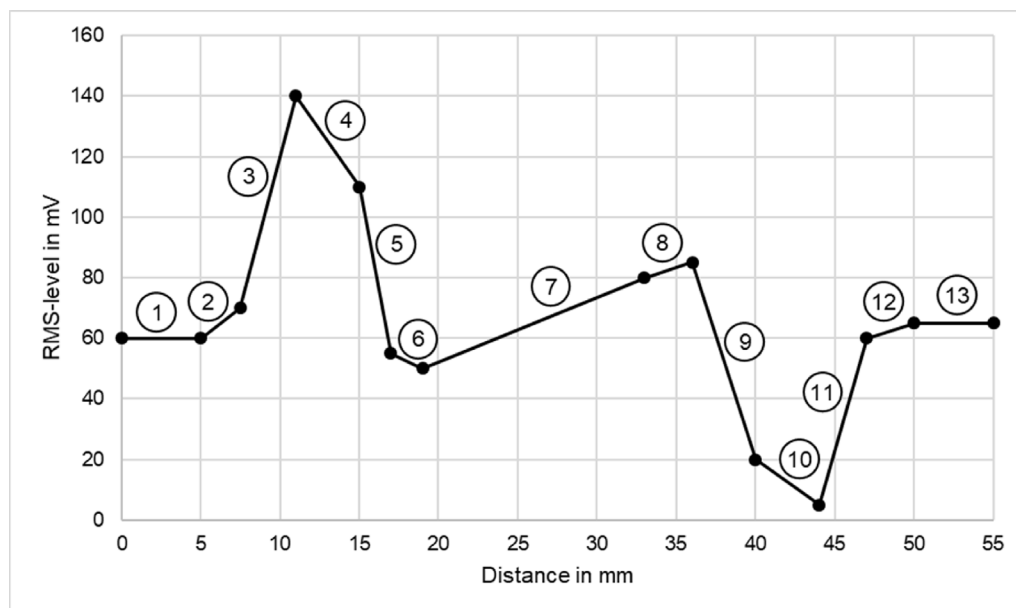
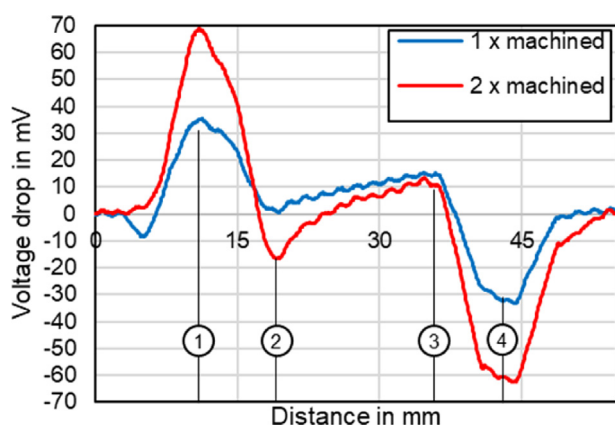**Fig. 21.** Schematic voltage behavior of E-core sensor at continuous feed.

Fig. 22. Real voltage behavior of E-core sensor at continuous feed and different surface treatments.

6. Conclusion

Several aspects have been investigated in this paper. The crystal structure of metastable austenitic steels and how it is affected by external strain, as well as the correlation to a change hardness as well as magnetic properties, a machining process to induce external strain and trigger microstructural changes and conventional as well as new approaches to determine and quantify these changes. Based on the knowledge gained, the following points can be concluded:

- MHP induces martensitic crystal structure which increases hardness and magnetic permeability in metastable austenitic materials.
- A smaller hammer head diameter correlates to a higher energy input, forming more martensite and increasing hardness further.
- The surface integrity can be determined by measuring the magnetic permeability, this is confirmed using classical measurement methods.

- The feritscope shows best correlation of α' values to the hardness measurements.
- Using the E-core sensor, edge detection as well as intensity detection of the MHP-treated areas is possible
- This approach allows permanent coding by altering the magnetic properties of metastable materials to a depth of hundreds of micrometers

7. Data availability

The raw/processed data required to reproduce these findings cannot be shared at this time due to technical or time limitations.

CRediT authorship contribution statement

Stephan Krall: Conceptualization, Methodology, Data curation, Investigation, Software, Validation, Visualization, Writing – original draft, Writing – review & editing, Project administration. **Markus Prießnitz:** Data curation, Investigation, Software, Validation, Visualization, Writing – original draft, Writing – review & editing. **Christian Baumann:** Data curation, Visualization, Writing – original draft, Writing – review & editing. **Friedrich Bleicher:** Funding acquisition, Supervision, Writing – review & editing.

Data availability

Data will be made available on request.

Declaration of Competing Interest

The authors declare that they have no known competing financial interests or personal relationships that could have appeared to influence the work reported in this paper.

Acknowledgments

Materials Science and Technology and the electron microscopy facility of TU Wien (USTEM) as well as the Machine Tool Technologies Research Foundation (MTTRF) and DMG MORI SEIKI for their support.

References

[1] V. Schulze, F. Bleicher, P. Groche, Y.B. Guo, Y.S. Pyun, Surface modification by machine hammer peening and burnishing, CIRP Ann. 65 (2) (2016) 809–832, https://doi.org/10.1016/j.cirp.2016.05.005.

[2] E. Brinksmeier et al., Process Signatures - The Missing Link to Predict Surface Integrity in Machining, Procedia CIRP 71 (2018) 3–10, https://doi.org/10.1016/j.procir.2018.05.006.

[3] VDI, 'VDI 3416 Blatt 1 Maschinelles Oberflächenhämmern – Grundlagen'. 2018.

[4] H. Ghaednia, X. Wang, S. Saha, Y. Xu, A. Sharma, R.L. Jackson, A Review of Elastic-Plastic Contact Mechanics, Appl. Mech. Rev. 69 (6) (Nov. 2017), https://doi.org/10.1115/1.4038187 060804.

[5] K. L. Johnson, Contact Mechanics, 1st ed. Cambridge University Press, 1985. doi: 10.1017/CBO9781139171731.

[6] V. L. Popov, M. Heß, and E. Willert, Handbook of Contact Mechanics: Exact Solutions of Axisymmetric Contact Problems. Berlin, Heidelberg: Springer Berlin Heidelberg, 2019. doi: 10.1007/978-3-662-58709-6.

[7] D. Tabor, A simple theory of static and dynamic hardness, Proc. R. Soc. Lond. Ser. Math. Phys. Sci. 192 (1029) (1948) 247–274, https://doi.org/10.1098/rspa.1948.0008.

[8] A. Cherif, Y. Pyoun, B. Scholtes, Effects of Ultrasonic Nanocrystal Surface Modification (UNSM) on Residual Stress State and Fatigue Strength of AISI 304, J. Mater. Eng. Perform. 19 (2) (2010) 282–286, https://doi.org/10.1007/s11665-009-9445-3.

[9] S. Krall, M. Reiter, F. Bleicher, Influence of the machine hammer peening technology on the surface near material structure of stainless steel X5CrNi18-10, Mater. Today Proc. 5 (13) (2018) 26603–26608, https://doi.org/10.1016/j.matpr.2018.08.123.

[10] O.P. Maksimova, Martensite transformations: History and laws, Met. Sci. Heat Treat. 41 (8) (1999) 322–339, https://doi.org/10.1007/BF02474881.

[11] P.L. Mangonon, G. Thomas, The martensite phases in 304 stainless steel, Metall. Trans. 1 (6) (1970) 1577–1586, https://doi.org/10.1007/BF02642003.

[12] J. Scheil, 'Entwicklung von Austenitisch-Ferritischem Gusseisen (ADI) aus EN-JS2070: Mikrostruktur, mechanische Eigenschaften und deren Auswirkung auf die Oberflächenbearbeitung durch das Maschinelle Oberflächenhämmern', 2016.

[13] G. Yudhisthir, 'Radial Angetriebene Schlagverdichtungssystem', DE202015003249.

[14] M. Kranz, 'Werkzeug und Verfahren zum Aufbringen kleiner Schlagimpulse', DE102014107173A1.

[15] C. Loeckner, 'Klopfvorrichtung und -verfahren', DE102006033004.

[16] A. Järvenpää, M. Jaskari, A. Kisko, P. Karjalainen, Processing and Properties of Reversion-Treated Austenitic Stainless Steels, Metals 10 (2) (2020) 281, https://doi.org/10.3390/met10020281.

[17] E. Macherauch, H.-W. Zoch, Praktikum in Werkstoffkunde: 91 ausführliche Versuche aus wichtigen Gebieten der Werkstofftechnik, 11, Vollständig überarbeitete und erw, Aufl, Vieweg+Teubner, Wiesbaden, 2011.

[18] M.J. Sohrabi, M. Naghizadeh, H. Mirzadeh, Deformation-induced martensite in austenitic stainless steels: A review, Arch. Civ. Mech. Eng. 20 (4) (2020) 124, https://doi.org/10.1007/s43452-020-00130-1.

[19] M. Naghizadeh, H. Mirzadeh, Effects of Grain Size on Mechanical Properties and Work-Hardening Behavior of AISI 304 Austenitic Stainless Steel, Steel Res. Int. 90 (10) (2019) 1900153, https://doi.org/10.1002/srin.201900153.

[20] T. Weiler, S. Krall, F. Bleicher, LINEAR RELUCTANCE ACTUATOR AND TOOLS/DRIVES DESIGNED TO COMPRISE SAME, WO2019096834 (2019).

[21] A. Abdi, H. Mirzadeh, M.J. Sohrabi, M. Naghizadeh, Phase Transformation Kinetics During Annealing of Cold-Rolled AISI 309Si Stainless Steel, Metall. Mater. Trans. A 51 (5) (2020) 1955–1959, https://doi.org/10.1007/s11661-020-05678-4.

[22] C. Loeckner, 'Verfahren und Vorrichtung zur kalten Mikroschmiedetechnik von beliebigen 3-D-Freiformflächen', DE112006002729, Jul. 10, 2008.

[23] C. Habersohn, Analytische und simulative Betrachtung eines Oberflächenhämmerprozesses, TU Wien (2015), https://doi.org/10.34726/HSS.2015.29836.

[24] M. Boniardi and Casaroli, Rostfreie Edelstähle. Politecnico di Milano, 2014.

[25] S. Ndlovu, K. Durst, M. Göken, Investigation of the sliding contact properties of WC-Co hard metals using nanoscratch testing, Wear 263 (7–12) (2007) 1602–1609, https://doi.org/10.1016/j.wear.2006.11.044.

[26] M. Pranger, Vergleich der Mikrostruktur ausgewählter hochfester Schweißungen, Montanuniversität Leoben, 2017.

[27] 'Ferrite Content Weld Seams | Ferrite Content Duplex Measurement', Ferrite Content Weld Seams | Ferrite Content Duplex Measurement. https://www.helmut-fischer.com/techniques/ferrite-content-measurement (accessed Jan. 11, 2023).

[28] J. Talonen, P. Aspegren, H. Hänninen, Comparison of different methods for measuring strain induced α-martensite content in austenitic steels, Mater. Sci. Technol. 20 (12) (2004) 1506–1512, https://doi.org/10.1179/026708304X4367.

[29] J. Fava, F. Carabedo, C. Spinosa, and M. Ruch, 'Assessment of the amount of deformation induced martensite: a calibration curve for the Ferritoscope', presented at the 12th European Conference on Non-Destructive Testing (ECNDT 2018), Gothenburg, Aug. 2018.

Glossary

a: Distance of indentation
AC: Alternate current
aE: Elastic contact radius
bct: Tetragonal space centered cell
C: Carbon
CCPM: Color coded phase map
Cr: Chromium
Cu: Copper
d: Diameter
di: diameter of indent
dp: entire penetration depth
E: Youngs modulus
EBSD: Electron backscatter diffraction
EE: Elastic energy
Ek0: Kinetic energy at impact
EP: Plastic deformation energy
F: Force
f: Frequency
fcc: Face centered cubic cell
G: Free Enthalpy
Gmech: mechanical enthalpy
GRT: Enthalpy at room temperature
GS: Start enthalpy
h: Stroke
HV: Vickers hardness
IPF: Inverse pole figure
ln: Logarithm
M_d: Temperature limit for deformation induced martensitic transformation
MHP: Machine Hammer Peening
Mn: Mangan
Mo: Molybdenum
M_S: Martensite starting temperature
$M_{S,\sigma}$: Temperature limit for stress induced martensitic transformation
m_{WZ}: Indenter mass
n: Number of machining passes
N: Newton
Ni: Nickel
p0: Hertz pressure
RMS: Root Mean Square
r_1: Indenter radius
r_2: Indentation radius
R^2: Coefficient of determination
Ra: Arithmetic average roughness value
RMS: Root mean square
RT: Room temperature
Rz: Mean roughness depth
s: Stepover distance
SN: Sample number
t: Time
T: Temperature
T_{trans}: Martensite transition temperature
tp: Depth of indentation
v: Feed rate
v_0: Impact velocity
v_Y: Velocity for yield
WC-Co: tungsten carbide
Y: Yield strength
α': Strain induced martensite phase
αM%: Percentage of α-martensite
Δ_{gmech}: Differential mechanically introduced enthalpy
Δ_{GRT}: Differential enthalpy cooling room temperature
Δ_{GS}: Differential starting enthalpy
Δ_T: Temperature difference
v: Poisson's ratio
ρ: Density
φ: Forming degree
μr: Relative permeability